energy&fuels

pubs.acs.org/EF

Article

$CuInS_2$ Nanosheet Arrays with a MoS_2 Heterojunction as a Photocathode for PEC Water Splitting

Mohit Kumar, Bhagatram Meena, Palyam Subramanyam, Govind Ummethala, Sai Rama Krishna Malladi, Shourya Dutta-Gupta, and Challapalli Subrahmanyam*

Cite This: *Energy Fuels* 2023, 37, 2340−2349

Read Online

ACCESS | Metrics & More | Article Recommendations | Supporting Information

ABSTRACT: Developing cost-effective noble metal-free co-catalysts as alternatives to platinum group metals is an impeccable strategy to enhance photoelectrochemical (PEC) water splitting. In this report, we successfully fabricated $CuInS_2$ nanosheet array-based photocathode modified with CdS and co-catalyst MoS_2 in a green approach to improve water splitting under solar irradiation. The visible light absorption of the modified hybrid photocathode ($CIS/CdS/MoS_2$) was significantly enhanced due to introducing CdS and MoS_2. Photoluminescence, impedance spectroscopy, and Mott−Schottky analysis depicted improved separation of excited electron−hole pairs, minimized resistance of charge transfer, and increased excited-state charge carrier concentration, resulting in increased photocurrent. Typical results indicated that composite photoelectrodes delivered higher photocurrent (−1.75 mA/cm^2 at 0 V vs RHE) and HC-STH conversion efficiency (0.42% at 0.49 V vs RHE) than those of CIS and CIS/CdS photoelectrodes. This improved PEC performance is accredited to the synergetic impact of CdS in charge generation and transfer and MoS_2 as a cocatalyst with active surface sites for proton reduction. This study not only reveals the promising nature of $CuInS_2$-based light absorber photocathodes for solar energy utilization but also recommends the use of MoS_2 as a cocatalyst for the proton reduction reactions for widespread applications in solar to hydrogen conversion.

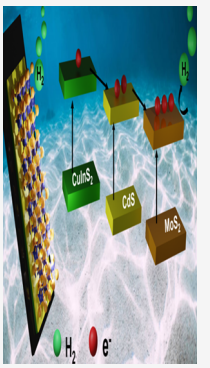

INTRODUCTION

Hydrogen is considered a clean fuel owing to its formidable energy density and zero carbon emission. It will be crucial in the near future as a renewable and sustainable energy source to meet the global energy demand.[1] Photoelectrochemical (PEC) water splitting offers a sustainable route to absorb sunlight falling on the earth's surface and use it to produce hydrogen from semiconducting metal oxides. Since Honda and Fujishima's pioneering work with TiO_2 photoelectrodes in 1972,[2] PEC water splitting has attracted considerable attention for exploring appropriate semiconductor materials as photoelectrodes. A number of n-type semiconductors, particularly TiO_2, WO_3, $BiVO_4$, and g-C_3N_4, have been explored as photoanodes for oxygen evolution in PEC cells for water splitting.[3,4] Hydrogen evolution takes place on p-type photocathodes, such as Cu_2O, CuO, $CuBi_2O_4$, $CuInS_2$, and $CuInGaS_2$ (CIGS).[5,6]

To date, p-type semiconductors have been less explored because of their high cost and low photostability. Recently, copper-based ternary semiconductors have shown potential application with high efficiencies due to their abundant resources, low cost, and tunable light absorption.[5] Among these Cu-based semiconductors, the $CuInS_2$ (CIS) photocathode has attracted great attention due to its non-toxicity, suitable optical direct band gap (E_g 1.4−1.9 eV), reasonable absorption coefficient, and high carrier concentration under illumination.[7] Gunawan and co-workers synthesized the CIS photocathode via electrodeposition that exhibited a photocurrent density of −0.51 mA/cm^2 at 0 V vs RHE.[8] Nonetheless, the photoactivity of the CIS photocathode is confined by its inherent properties; for instance, photocorrosion, high charge recombination, and short carrier diffusion. Numerous strategies have been developed to suppress the recombination and enhance the disassociation of the photo-induced charge carriers, including doping,[9] structure control,[10] heterojunction construction,[11] plasmonic metal NPs,[6] and co-catalyst loading.[12,13] Recently, Moon et al. demonstrated the anodized aluminum oxide template-based CIS nanorods that were vertically aligned and modified with CdS and ZnS deposition. The modified photoelectrodes demonstrated PEC performance displaying a photocurrent of −2 $\mu A/cm^2$ and flat-band potential shift from pure CIS.[14] Recently, Liu et al. reported $CIS/Sb_2S_3/Pt$ heterostructure photocathodes exhibited a photocurrent density of −2.48 mA/cm^2 at −0.6 V vs RHE, which is 3.13 times greater in contrast to that of pure CIS photocathode.[15] The heterojunction structure improves the conversion efficiency and allows the selection of semiconductors with a broad range of light absorption. Metal sulfides, like In_2S_3,[16] CdS,[17,18] ZnS,[19] and

Received: October 18, 2022
Revised: January 7, 2023
Published: January 23, 2023

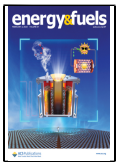

https://doi.org/10.1021/acs.energyfuels.2c03502
Energy Fuels 2023, 37, 2340−2349

Scheme 1. Fabrication Scheme of FTO/CIS/CdS/MoS_2 Photoelectrode

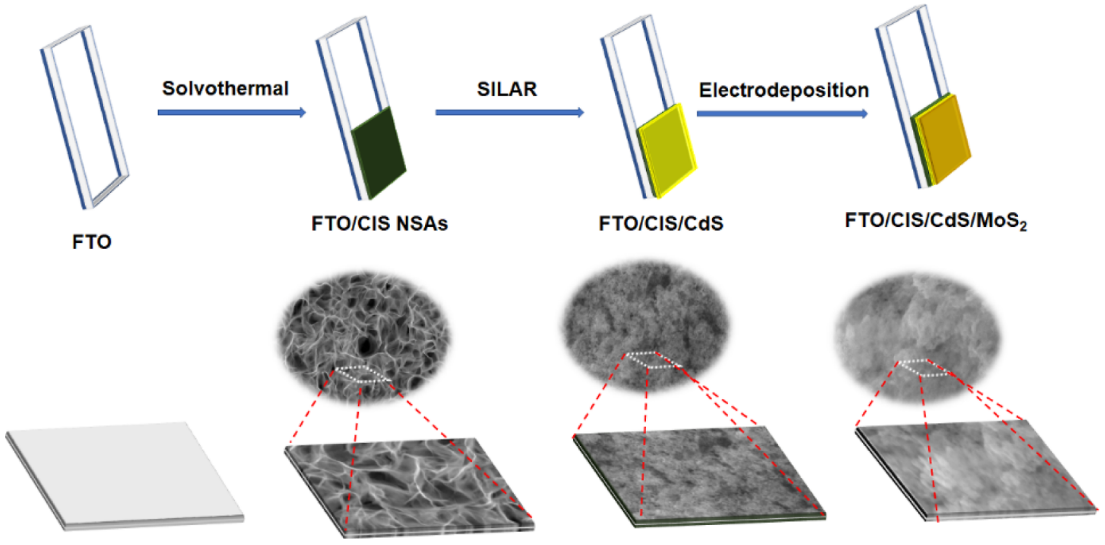

Sb_2S_3,[20] have been widely used to construct heterojunctions with CIS because of their suitable band alignment for excited-state charge transfer. Ikeda et al. fabricated a CZTS/CdS/In_2S_3/Pt photoelectrode for water splitting with a high photocurrent of −4.5 mA/cm^2 and a low onset potential. In addition, CdS was stabilized against photodegradation by the deposition of In_2S_3.[21] Li et al. demonstrated the $CuInS_2$/CdS heterojunction yielded a higher photocurrent density (−0.25 mA/cm^2 at 0 V vs RHE) than pristine $CuInS_2$ electrode.[22] The Cu_2O photocathode suffers from photocorrosion, which limits its faradaic efficiency for hydrogen evolution reaction (HER) (∼0.01%). Septina et al. fabricated a FTO/Au/Cu_2O/CdS/TiO_2/Pt photocathode using a CdS buffer layer and champion electrode and exhibited −1.68 mA/cm^2 at 0 V vs RHE and onset potential of 0.45 V vs RHE, which generated H_2 with a faradaic efficiency of ∼100% in 1 M kPi buffer (pH 7).[23] Cation exchange reaction, where Cd^{2+} is replaced by Cu^+, was recently reported forming an inherent Cu_2S/CdS heterojunction.[24]

On the other hand, co-catalyst loading improves the kinetics of the charge transfer to the semiconductor−electrolyte interface, which significantly enhances the performance of PEC water splitting and stability of the photoactive electrode. Typically, noble metals like Pt,[25] Au,[26] and RuO_2[27] are widely used as co-catalysts that catalyzes HER. However, an extensive and vast range of diverse applications of these noble metal catalysts is limited by their low abundance and high price, which hinders the widespread use of solar-driven PEC water splitting. Alternatively, researchers aim to develop low-cost and earth-abundant co-catalysts with improved activity from non-precious metallic oxides/sulfides. For example, Liu and Zhou modified the pristine CIS photoelectrode with nickel oxide (NiO) and nickel sulfide (NiS) as a hole transporting layer and co-catalyst, respectively. The results show that the NiS/$CuInS_2$/NiO heterostructured photocathode showed a photocurrent density of −2.23 mA/cm^2 at −0.6 V vs RHE, which is 175% higher in comparison to the $CuInS_2$ photocathode.[28] In recent years, among various transition-metal dichalcogenides, molybdenum disulfide (MoS_2) has been considered as a promising material with a wide range of applications in batteries, photodetectors, supercapacitors, gas detectors, and solar cells[29] Typically, MoS_2 has unique properties, such as good thermal stability, superior electrochemical performance, and a homologous-layered structure.[30] In addition, the HER proton acceptor sites on the surface of MoS_2 provides a unique catalytic site for proton reduction, which reduces the activation energy barrier for HER to proceed.[31,32] Previously, Yuan et al. fabricated a MoS_2/$CuInS_2$ heterojunction photocatalyst for H_2 evolution in basic conditions using Na_2S/Na_2SO_3 sacrificial reagents in the electrolyte. 3 wt % MoS_2/$CuInS_2$ electrode shows the highest photocurrent density of 7.8 μA/cm^2, which is about 7 times higher than that of the bare $CuInS_2$ electrode.[33] Recently, Qin et al. fabricated a photodetector using the MoS_2−$CuInS_2$-AuNP 2D−0D hybrid, where a facile electron movement from $CuInS_2$ to MoS_2 showing excellent photoresponse compared to $CuInS_2$ due to an enhanced electric field.[34] Sellappan and Varunkumar fabricated the $CuBi_2O_4$/MoS_2 photocathode delivered a high photocurrent value of −0.182 mA/cm^2 than pristine $CuBi_2O_4$ (−0.082 mA/cm^2 at 0.6 V vs RHE) owing to the presence of MoS_2.[35] Recently, Dolai et al. developed a MoS_2@CdS heterojunction photocathode with a photocurrent density of −6.45 mA/cm^2 at −0.5 V vs RHE. This improvement was attributed to the presence of MoS_2, which improved the photostability, charge carrier separation, and transport.[30] The heterojunction of CIS and CdS due to the favorable band alignment makes it very beneficial for charge separation and transport and decorating the overlayer of cost-effective co-catalyst like MoS_2 might be of great potential for solar-harvesting module.

In this study, we have successfully fabricated CdS/MoS_2-sensitized CIS nanosheet arrays (NSAs) for solar hydrogen evolution. Fabricating heterojunction and incorporating noble metal-free co-catalysts improved the PEC performance. The porous CIS NSAs were synthesized via the solvothermal synthesis followed by deposition of CdS through successive ionic layer adsorption reaction (SILAR) and MoS_2 electrodeposited over CIS/CdS. PEC performance of porous 2D-entangled nanosheets of CIS NSAs with a high surface area (59 m^2/g) ameliorated on the deposition of CdS forming a p−n heterojunction. Deposition of non-noble metal cocatalyst (MoS_2) forming CIS/CdS/MoS_2 imparted stability to the photoelectrode with no significant decay in the photocurrent even after 6 h of continuous operation. The resulting CIS/CdS/MoS_2 nanocomposite photocathode showed a higher

https://doi.org/10.1021/acs.energyfuels.2c03502
Energy Fuels 2023, 37, 2340−2349

photocurrent response and superior stability compared to CIS, CIS/CdS, and CIS/MoS_2 photocathodes. The hydrogen evolution experiment showed CIS/CdS/MoS_2 (56.9 μmol/h) showed high activity and rate of hydrogen evolution compared to CIS (22.6 μmol/h). CdS and MoS_2 synergistically decreased the charge recombination, amplified light absorption, and increased the charge carrier concentration, resulting in an increase in PEC−HER of CIS NSAs.

EXPERIMENTAL SECTION

Fabrication of FTO/CIS NSA Photocathode. CIS NSAs were grown onto the FTO film using the solvothermal method. In brief, $CuCl_2{\cdot}2H_2O$ (0.1 mM), $InCl_3{\cdot}4H_2O$ (0.25 mM), and thioacetamide (0.75 mM) were used as Cu, In, and S precursors, respectively, and all precursors are dispersed/dissolved in ethanol (15 mL). The resulting solution was poured into a Teflon-lined autoclave followed by pre-cleaned FTO plates were kept in a Teflon tube with the conductive side toward the wall of the tube. The reaction proceeded at 180 °C for 8 h. After the reaction, the obtained FTO/CIS samples were washed four times with DI water and absolute ethanol to remove loosely bound impurities and annealed at 300 °C for 1 h in an inert argon (Ar) environment(Scheme 1).

Fabrication of FTO/CIS/CdS Photoelectrode. A CIS/CdS photoelectrode was fabricated using the SILAR method. Briefly, the CIS/FTO film was immersed in the Cd precursor solution [$Cd(OAc)_2{\cdot}2H_2O$ (0.1 M) in methanol] for 30 s and then rinsed in methanol to remove the loosely bound ions and subsequently dried at 70 °C for 2 min. Further, those films were soaked in a sulfide precursor solution (0.1 M $Na_2S{\cdot}xH_2O$ in CH_3OH)) for 30 s, followed up by washing with methanol and kept for drying at 70 °C for 2 min. Finally, all steps constitute one SILAR cycle. Similarly, 5, 10, and 15 SILAR cycle sequences were carried out to attain the desired CIS/CdS-5, CIS/CdS-10, and CIS/CdS-15 photoelectrodes, respectively (Scheme 1). The CIS/CdS films were annealed at 300 °C in an Ar environment for 1 h.

Fabrication of FTO/CIS/MoS_2 Photoelectrode. MoS_2 layer was deposited over FTO/CIS using the electrodeposition method. First, the MoS_4^{2-} solution was processed by adding aqueous solution of Na_2MoO_4 (5 mM) and Na_2S (excess) followed by dil. HCl was added dropwise to pH 8. After the addition of dil. HCl, the clear solution was changed to dark, indicating the formation of MoS_4^{2-} solution.

$$MoO_4^{2-} + 4H_2S \rightarrow MoS_4^{2-} + 4H_2O$$

Typically, an electrodeposition process proceeds with a three-electrode system, where FTO/CIS as the working electrode, Ag/AgCl as the reference electrode, Pt as the counter electrode, and MoS_4^{2-} solution served as the electrolyte for MoS_2 deposition. The deposition was performed at −1.2 V for 10 min to attain the brown color of the FTO/CIS/MoS_2 electrode. Cyclic voltametric curve for the electrodeposition can be found in Supporting Information, Figure S10b. The films were heated at 300 °C in an Ar environment for 1 h. The electrolytic reduction of the tetrathiomolybdate ion (MoS_4^{2-}) proceeds in the following manner

$$MoS_4^{2-} + 2e^- + 2H_2O \rightarrow MoS_2 + 2HS^- + 2OH^-$$

Fabrication of FTO/CIS/CdS/MoS_2 Photoelectrode. The MoS_2 layer was deposited over FTO/CIS/CdS using the electrodeposition method. First, the MoS_4^{2-} solution was processed by adding aqueous solution of Na_2MoO_4 (5 mM) and Na_2S (excess) followed by dil. HCl was added dropwise to pH 8. After the addition of dil. HCl, the clear solution was changed to dark, indicating the formation of MoS_4^{2-} solution.

$$MoO_4^{2-} + 4H_2S \rightarrow MoS_4^{2-} + 4H_2O$$

Typically, an electrodeposition process proceeds with a three-electrode system, where FTO/CIS/CdS as the working electrode, Ag/AgCl as the reference electrode, Pt as the counter electrode, and MoS_4^{2-} solution served as the electrolyte for MoS_2 deposition (Supporting Information, Figure S10b). The deposition was performed at −1.2 V for 10 min to attain the brown color of the FTO/CIS/CdS/MoS_2 electrode (Scheme 1). The films were heated at 300 °C in an Ar environment for 1 h. The electrolytic reduction of the tetrathiomolybdate ion (MoS_4^{2-}) proceeds in the following manner

$$MoS_4^{2-} + 2e^- + 2H_2O \rightarrow MoS_2 + 2HS^- + 2OH^-$$

RESULTS AND DISCUSSION

Crystallographic and Morphological Studies. X-ray diffraction (XRD) patterns of the synthesized parent material and modified photocathodes were analyzed to probe the phase and crystallographic structure of the materials. In the pristine CIS NSAs, the diffraction pattern peak 2θ values at 27.6, 31.4, 46.2, and 55° correlate with (112), (004), (202), (211), (204), (116), and (312) planes at the d-spacings of 3.2, 2.76, 2.44, 2.41, 1.95, 1.67, and 1.66 Å, respectively, which are in good agreement with body-centered tetragonal crystalline CIS (JCPDS no. 32-0339) (Figure 1). In the diffraction pattern

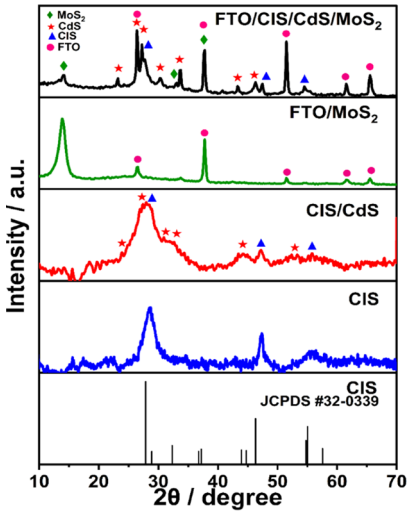

Figure 1. XRD diffraction characteristics of pristine CIS NSAs, CIS/CdS, and FTO/CIS/CdS/MoS_2 and CIS JCPDS no. 32-0339.

of CdS, the 2θ peak values at 26.9, 30.5, 44.5, and 52.7° correspond to the (111), (200), (220), and (311) planes with d-spacings of 3.4, 2.90, 2.05, and 1.75 Å, respectively, which is consistent with JCPDS no. 80-0019 (Supporting Information, Figure S1). For the CIS/CdS composite, both CIS and CdS peaks are observed in Figure 1. This suggests that the CdS layers were successfully decorated onto the CIS surface and certifies the formation of the CIS/CdS heterostructure. The XRD patterns of FTO/MoS_2 show three peak 2θ values of 14.2, 32.8, and 39.4° corresponding to (002), (100), and (103) planes at d-spacings of 6.15, 2.73, and 2.27 Å, respectively, which matched with the hexagonal structure of MoS_2 (JCPDS card no. 37-1492) (Supporting Information, Figure S1). The XRD pattern of FTO/CIS/CdS/MoS_2 composite shows the marked peaks corresponding to CIS (▲), CdS(★), and MoS_2 (◆) along with FTO (●) peaks (Figure 1), which confirmed the formation of composites.

The surface morphology of CIS NSAs, CIS/CdS, and CIS/CdS/MoS_2 was studied using FE-SEM (Figure 2). CIS reveals an exfoliated graphene sheet-like structure with porosity and high surface area (like 2D NSAs), which are highly

https://doi.org/10.1021/acs.energyfuels.2c03502
Energy Fuels 2023, 37, 2340−2349

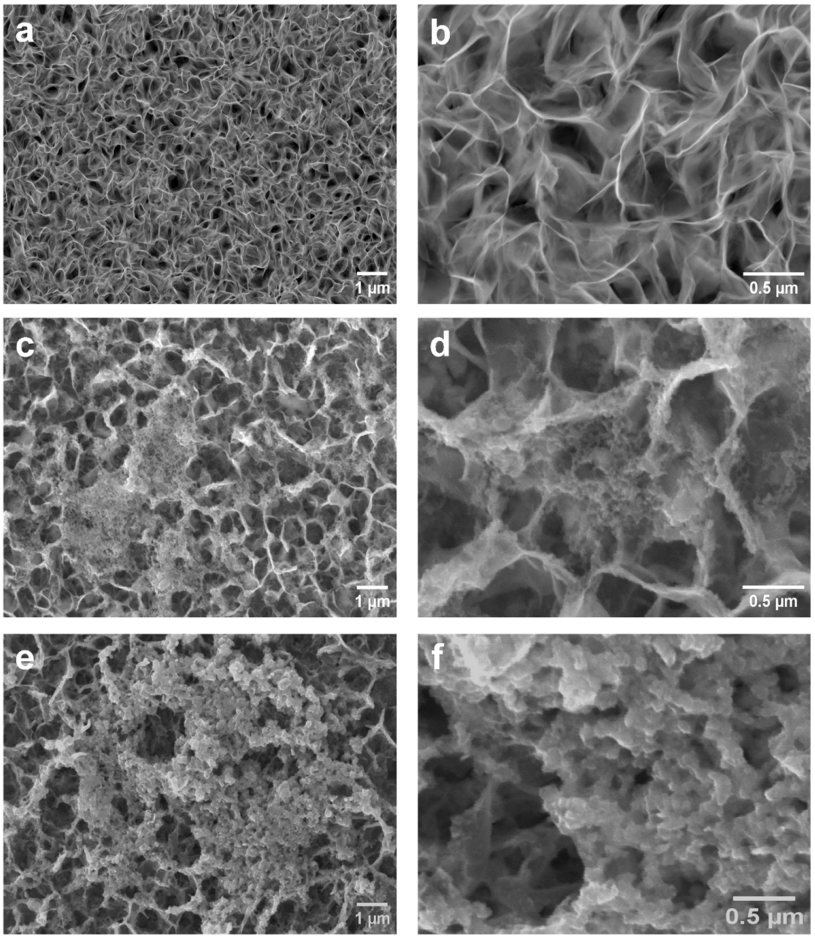

Figure 2. SEM images of (a) CIS NSAs; (b) magnified image of CIS NSAs (c); CIS/CdS; (d) magnified image of CIS/CdS heterojunction; (e) CIS/CdS/MoS_2; and (f) magnified image of CIS/CdS/MoS_2 composite.

interconnected and vertically grown onto the FTO substrate (Figure 2a,b). A ratio of $[Cu^{+2}]/[In^{+3}]$ = 0.4 has shown a continuous- and pristine-entangled nanosheet morphology along with enhanced absorption and photocurrent density. The $[Cu^{+2}]/[In^{+3}]$ ratios ≤0.2 and ≥0.9 have shown a less porous and broken nanosheet morphology.[36] The pristine CIS exhibits nanosheet morphologies with an average sheet width of 25.9 nm using the size distribution (Supporting Information, Figure S2). Keeping in mind the porosity and surface area of CIS NSAs, Brunauer−Emmett−Teller (BET) analysis revealed the surface area, average pore diameter, and total pore volume of synthesized CIS NSAs. The N_2 adsorption and desorption isotherms of the as-prepared CIS NSAs after annealing in an Ar atmosphere at 300 °C for 1 h depicted type-IV with a H3-type hysteresis loop in the range of 0.4−0.95 P/P_0. The surface area of $CuInS_2$ NSAs was calculated to be 59.3 m^2/g (Supporting Information, Figure S3) having an average pore radius of 47.4 Å and total pore volume of 1.4 cm^3/g. This hierarchical entangled and porous nanosheet morphology facilitates the charge transfer from its surface to the CdS and endows it with a greater surface area for adequate light harvesting. CdS deposited over CIS in CIS/CdS, the heterojunction of CdS uniformly distributed over CIS can be observed in Figure 2c,d. The electrodeposited MoS_2 over CIS/CdS resulted in epitaxial growth of exfoliated multi-layered MoS_2 nanosheets, heterojunction of CIS/CdS/MoS_2 can be observed in Figure 2e,f. Sheet-like MoS_2 passivates the surface of CIS/CdS and provide stability toward photocorrosion. Further, we also calculated the atomic % using EDAX analysis for CIS, CIS/CdS, and CIS/CdS/MoS_2. It was found that the ratio of atomic % remains constant for all elements after every successive deposition of another layer and matched well with the synthetic precursors used for synthesis (Supporting Information, Figures S4−S6). The cross-sectional view of the films was examined for the conformation of heterostructure formation and measured the thickness of the layers, respectively (Supporting Information, Figure S7). The thickness of the layer in CIS/CdS/MoS_2 were calculated to be 0.6, 0.4, and 0.5 μm corresponding to MoS_2, CdS, and CIS, respectively.

The micromorphological properties of the CIS/CdS/MoS_2 composite structure were probed by TEM (Figure 3). The low-magnification TEM micrograph (Figure 4a) depicts the presence of CdS and MoS_2 over the CIS nanosheets, which agrees with the outcome of SEM results. Moreover, high-resolution TEM micrographs (Figure 3b) displayed the crystalline nature of the CIS NSAs having continuous well-distinguished lattice fringes with a spacing of 0.32 nm correlated to the (112) planes, which is in excellent agreement with the most substantial peak of the XRD pattern, 2θ = 27.6°, and a lattice spacing of 0.34 nm matching with the (111) plane of CdS located at 2θ = 26.9°. In the micrograph in Figure 3c, a lattice spacing of 0.22 nm corresponds to the (103) surface of MoS_2. Furthermore, EDS mapping was used to confirm the presence and uniform distribution of CdS and MoS_2 over CIS

https://doi.org/10.1021/acs.energyfuels.2c03502
Energy Fuels 2023, 37, 2340−2349

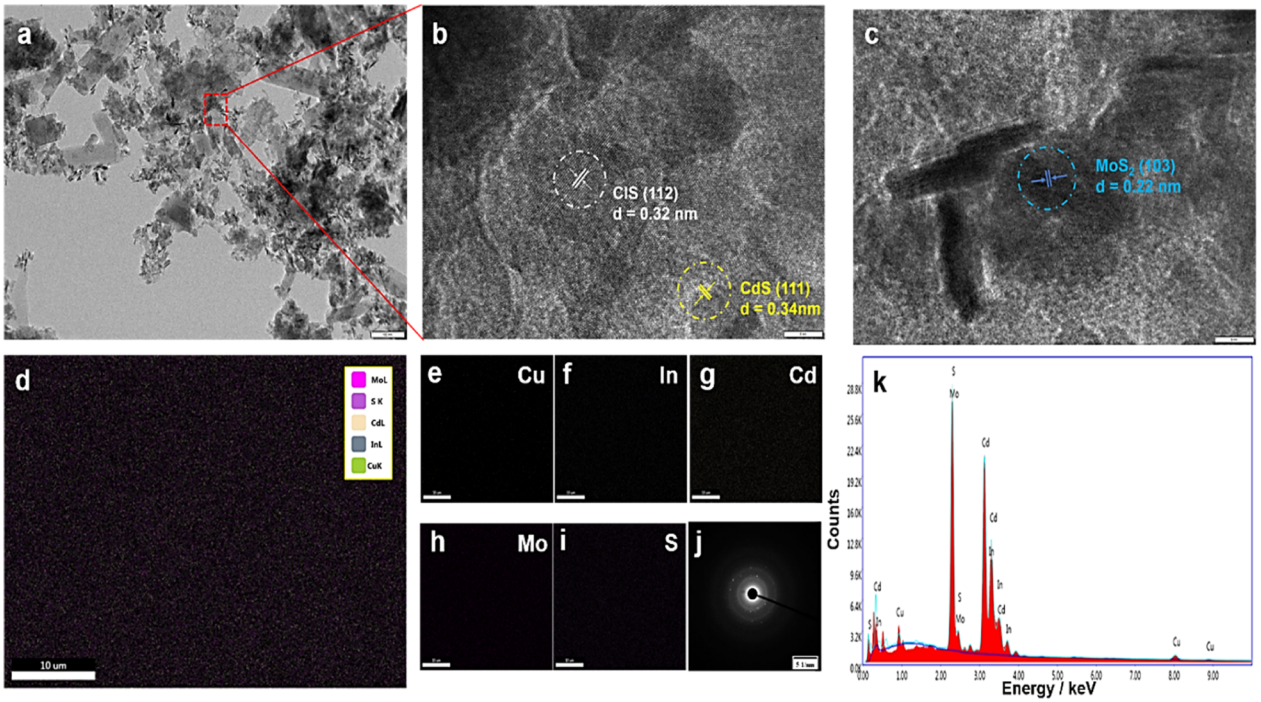

Figure 3. (a) Low-resolution TEM micrograph of CIS/CdS/MoS_2; (b,c) high-resolution images of CIS/CdS/MoS_2 composite; (d) EDS elemental mapping of CIS/CdS/MoS_2 composite; (e−i) elemental mapping of Cu, In, Cd, Mo, and S, respectively; (j) SAED pattern obtained from the CIS/CdS/MoS_2 composite; and (k) EDS spectra of Cu, In, Cd, Mo, and S for the CIS/CdS/MoS_2 composite.

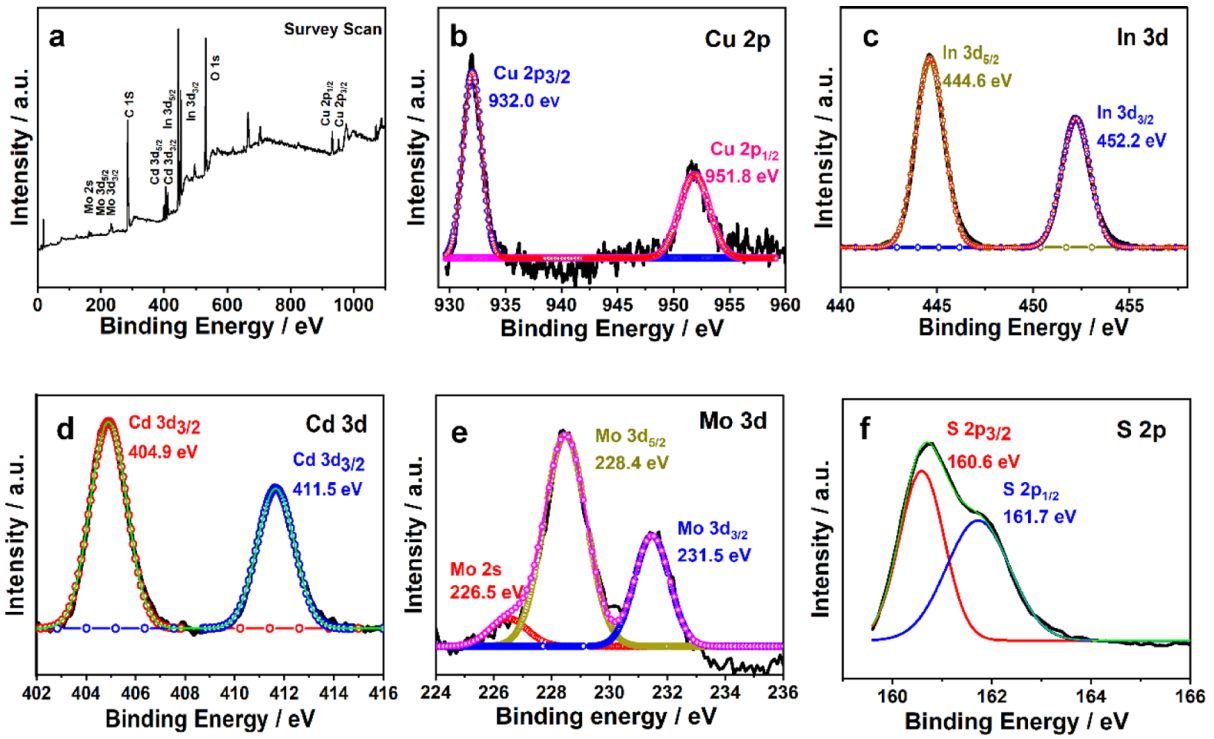

Figure 4. XPS spectrum of CIS/CdS/MoS_2: (a) survey scan; (b) Cu 2p; (c) In 3d; (d) Mo 2s and 3d; (e) Cd 3d; and (f) S 2p.

NSAs in the CIS/CdS/MoS_2 photocathode (Figure 3d−i). The SAED pattern of the CIS/CdS/MoS_2 shows the polycrystalline nature of the CIS/CdS/MoS_2 composite (Figure 3j). EDS spectra certify the presence of Cu, In, Cd, Mo, and S elements in the composite (Figure 3k).

X-ray photoelectron spectroscopy (XPS) is used to describe and portray the surface chemical constituent elements and their valence state of elements present in the composite. The binding energy peaks of Cu $2p_{1/2}$ and Cu $2p_{3/2}$ are centered at 951.85 and 931.9 eV, respectively (Figure 4b). These values match with the typical data values reported in the literature. The XPS of In exhibits two peaks at 452.1 and 444.6 eV, which are analogous to In $3d_{3/2}$ and In $3d_{5/2}$, accordingly (Figure 4c).[10] The XPS spectrum of Cd shows that peaks at 411.6 and

https://doi.org/10.1021/acs.energyfuels.2c03502
Energy Fuels 2023, 37, 2340−2349

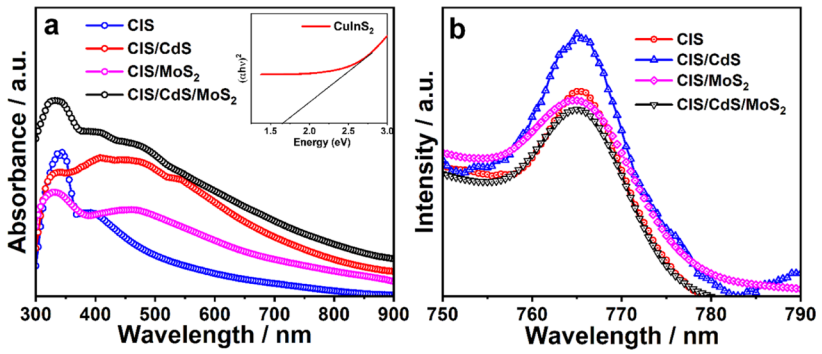

Figure 5. (a) UV−vis spectra of CIS NSAs, CIS/CdS, CIS/MoS_2, and CIS/CdS/MoS_2 composites and (b) PL spectra of CIS NSAs, CIS/CdS, CIS/MoS_2, and CIS/CdS/MoS_2 composites.

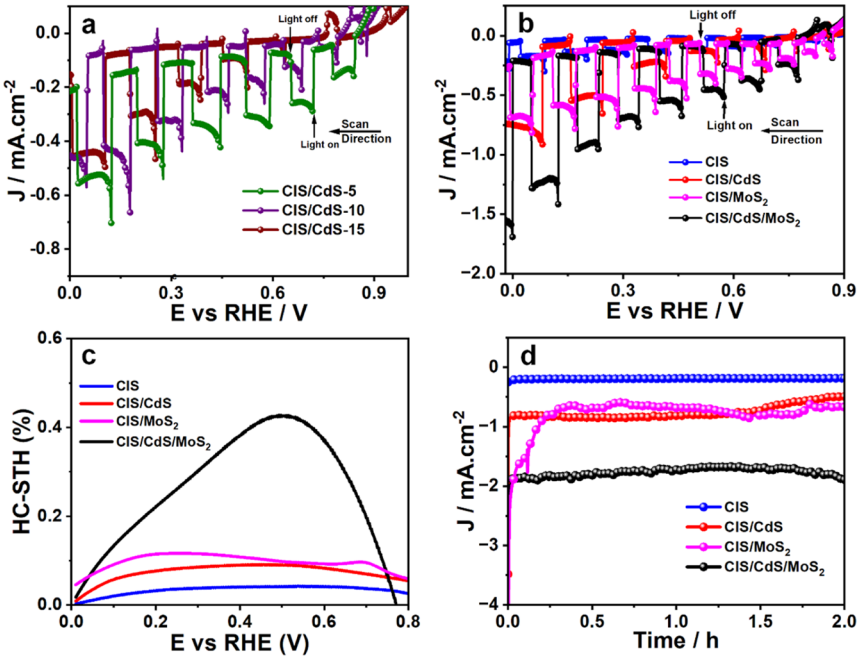

Figure 6. (a) LSV curves of CIS/CdS-5 and CIS/CdS-10 photocathodes under chopped illumination; (b) LSV curves; (c) HC-STH efficiency of pristine CIS NSAs, CIS/CdS, CIS/MoS_2, and CIS/CdS/MoS_2 photocathodes under chopped illumination; and (d) chronoamperometric (I−t) curves of pristine CIS NSAs, CIS/CdS, CIS/MoS_2, and CIS/CdS/MoS_2 photocathodes at 0 V vs RHE under light illumination.

405 eV are related to Cd $3d_{3/2}$ and Cd $3d_{5/2}$ (Figure 4d).[37] The Mo XPS spectrum showed three peaks at 231.5, 228.4, and 226.5 eV designated to Mo $3d_{3/2}$, Mo $3d_{5/2}$, and Mo 2s (Figure 4e).[38,39] The XPS peak of the S 2P core splits into two peaks, 161.7 and 160.6 eV, belonging to S $2p_{1/2}$ and S $2p_{3/2}$, respectively (Figure 4f). In accordance with the XPS data measurements, the binding energies of the corresponding elements are in total agreement with the studies in the literature. Therefore, XPS confirms the composition of the heterostructure fabricated on FTO.

Optical Studies. We examined the optical absorption characteristics of the fabricated photoelectrodes, and the outcomes are expressed in Figure 5. The pristine CIS NSAs show a broad absorption range of 300−765 nm (Figure 5a), and the band gap is estimated to be E_g = 1.62 eV by the Tauc's plot (inset Figure 5a). CdS clearly reveal a narrow spectral width with an absorption edge at 564 nm, having a band gap of 2.2 eV calculated using the Tauc's plot (Supporting Information, Figure S8b). Further, the CIS/CdS composite manifests a wide-ranging absorption range in the 300−800 nm range and a red shift in absorption spectra compared to CIS NSAs (Figure 5a). CIS/MoS_2 absorption enhanced as compared to CIS in the visible region owing to MoS_2 deposition. On the modification of the CIS/CdS electrode using the MoS_2 layer, the absorption band of the electrode extended and improved the absorption intensity over other electrodes (Figure 5a), resulting in improved light trapping capability. This intensified optical absorption leads to the production of electron−hole pairs, which increases the charge-carrier density; in the wavelength range where there exists a weak absorption of CIS NSAs.

Furthermore, PL studies were conducted to understand the recombination and charge-transfer response of the heterostructure photoelectrodes. The PL spectra of bare CIS NSAs, CIS/CdS, and CIS/CdS/MoS_2 samples were excited at a wavelength of 587 nm, and outcomes are displayed in Figure 5b. The CIS NSAs show a broad emission peak at 765 nm, which correlates to a peak energy of 1.62 eV and is assigned to the near-band edge emission (Figure 5b). Furthermore, when CdS was introduced on the top of CIS, the intensity of the

https://doi.org/10.1021/acs.energyfuels.2c03502
Energy Fuels 2023, 37, 2340−2349

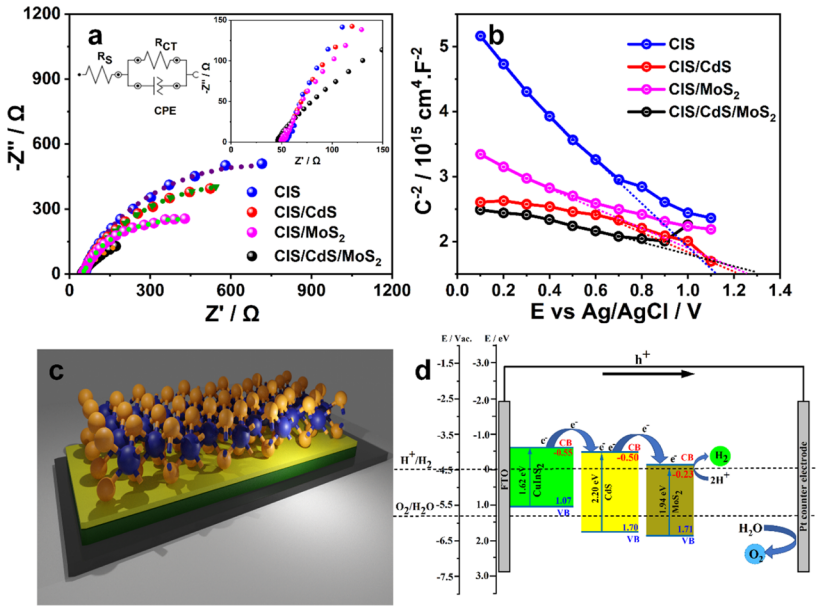

Figure 7. (a) Nyquist plots of pristine CIS NSAs, CIS/CdS, CIS/MoS_2, and CIS/CdS/MoS_2 photocathodes with circuit fitting and equivalent circuit (inset) measured at 0 V vs RHE and (b) Mott−Schottky plots of pristine CIS NSAs, CIS/CdS, CIS/MoS_2, and CIS/CdS/MoS_2 photocathodes. Schematic illustration; (c) photoelectrode FTO/CIS/CdS/MoS_2 [CIS (green), CdS (yellow), MoS_2 (crystal)] and (d) band gap alignment and the electron transfer with HER on the CIS/CdS/MoS_2 photocathode and OER on the counter electrode.

emission peak was significantly reduced. This intensity reduction performance certifies the excited-state communication of charges within CIS NSAs and CdS and is supported by the fact of deactivation by electron transfer of the excited state from CIS NSAs to CdS. This phenomenon implies that the photo-produced electron−hole pairs are effectively isolated in the CIS/CdS heterojunction. CIS/MoS_2 showed the reduced rate of recombination compared to CIS/CdS. Subsequently, PL spectra of the CIS/CdS/MoS_2 photoelectrode exhibited a decrease in intensity compared to CIS/CdS and CIS/MoS_2 photoelectrodes, satisfying the condition of the excited-state charge transfer along the heterojunction to the surface of the HER catalyst.

PEC Studies. The photoelectrocatalytic activity of the photoelectrodes was evaluated via J−V plots under the influence of solar irradiation at 100 mW/cm^2 (AM 1.5G). Also, we investigated the effect of the number of SILAR cycles of CdS deposition on CIS NSA on the photocurrent and examined J−V plots of CIS/CdS-5, CIS/CdS-10, and CIS/CdS-15 photoelectrodes (Figure 6a). Upon light illumination, the CIS/CdS-5 photocathode showed a more decent photocurrent response than the other electrodes. This effect could be accredited to proficient light absorption by virtue of the low scattering effect and low aggregation, which facilitated the charge separation of the excited states by effective heterojunction formation. Therefore, optimizing the CdS deposition cycles of the photocathode film is significant for high-performance PEC water splitting, and the optimized CIS/CdS-5 was used for further experiments. The LSV plots of CIS NSAs, CIS/CdS, and CIS/CdS/MoS_2 photoelectrodes are shown in Figure 6b. Under chopped light illumination, CIS NSAs, CIS/CdS, CIS/MoS_2, and CIS/CdS/MoS_2 photoelectrodes showed photocurrent densities of 0.28, 0.75, 0.81, and 1.75 mA/cm^2 at 0 V vs RHE, respectively. A minimal onset potential of 0.86 V and the highest photoresponse in terms of current density is observed for CIS/CdS/MoS_2, which is 6.2 times greater than pristine CIS NSAs, 2.3 times higher than the CIS/CdS photocathode, and 2.2 times higher than CIS/MoS_2. Similar results were obtained for LSV under continuous illumination of light (Supporting Information, Figure S9). The enhanced photocurrent density of the CIS/CdS/MoS_2 electrode is attributed to the synergetic effects of CdS, which has light sensitization ability, and MoS_2, which is known to be a good electrocatalyst with high conductivity. We also tested PEC performance of CdS/MoS_2 in 0.1 M Na_2SO_4 and it was found that CdS/MoS_2 showed the characteristics of a photoanode. CdS with different SILAR cycles (5 and 10 cycles) and MoS_2 with different deposition times (10 and 20 min) were fabricated and tested (Supporting Information, Figure S10a). The effect of MoS_2 deposition over the surface of CIS/CdS/MoS_2 was examined with varying times of electrodeposition. The electrodeposition at 5, 10, 15, and 20 min was fabricated and examined for PEC performance (Supporting Information, Figure S11). There was an increase in photocurrent observed for CIS/CdS/MoS_2-5 (1.03 mA/cm^2) and CIS/CdS/MoS_2-10 (1.75 mA/cm^2) but after 10 min of electrodeposition, the photocurrent decreases in CIS/CdS/MoS_2-15 (1.3 mA/cm^2) and CIS/CdS/MoS_2-20 (0.9 mA/cm^2 at 0 V vs RHE). The decrease in photocurrent density can be attributed to the parasitic light absorption from MoS_2, which increases with increasing deposition times of MoS_2 layer, making a MoS_2 layer of larger thickness. Decreased light availability to the photoactive layers leads to limited charge carrier generation which resulted in decreased photocurrent as can be seen in CdS/MoS_2 LSV curves. Moreover, the efficiency of a photoelectrode is stated in the context of STH conversion. The HC-STH conversion efficiencies for CIS NSAs, CIS/CdS, CIS/MoS_2, and CIS/CdS/MoS_2 are estimated to be 0.05, 0.10, 0.11, and 0.42%, respectively (Figure 6c). Impressively, the CIS/CdS/MoS_2 photoelectrode delivered a higher STH conversion efficiency than other electrodes. The increase in photocurrent can be associated with effective electron transfer to the surface, reducing the recombination probability. Moreover, the onset potential shifted toward a lower voltage

https://doi.org/10.1021/acs.energyfuels.2c03502
Energy Fuels 2023, 37, 2340−2349

for the CIS/CdS and CIS/CdS/MoS_2 compared to pristine CIS. The shift can be assigned to CdS layer deposition.

In order to assess the stability of the fabricated photocathodes, chronoamperometry was used. The photocurrent feedback of the photocathodic electrodes is time tested at 0 V vs RHE under light irradiation, and experimental outcomes are depicted in Figure 6d. The pristine CIS NSA photocathode unveiled a stable photocurrent response for over 2 h, while CIS/CdS displayed a stable photocurrent feedback up to 1.5 h, after which there was a decrease in photocurrent. This decrease in photocurrent may be a consequence of the dissolution of sulfur in the electrolyte. CIS/MoS_2 exhibited a stable photocurrent density of 0.8 mA/cm^2 for 2 h. The modified photocathode CIS/CdS/MoS_2 exhibited a stable photocurrent response with no decay in performance being observed after 2 h. To further check the stability of the stable photocurrent response to light, we also performed $I-t$ for 10 h at 0 V vs RHE (Supporting Information, Figure S12). CIS/CdS/MoS_2 showed a stable current for 6 h, after which decay in photocurrent was observed, which continued to decay gradually for 10 h of illumination. This significant increase and stability of the photocurrent were attributed to the surface passivation, which prevented the leaching of sulfur from CdS and increased the photocurrent by efficiently separating the excited electron−hole pairs. Furthermore, these results were consistent with the LSV curves. The constitution of a p−n heterojunction linking CIS NSA and CdS increases the photocurrent due to ameliorated charge separation and photoabsorption; the synergistic impact of CdS and MoS_2 is thought to enhance the photoactivity and increase the photocurrent due to surface passivation.

Further, charge injection kinetics at the photocathode−electrolyte interface is examined by evaluating the resistance across the interface of the electrode/electrolyte. Here, EIS experimental measurements were performed under the light illumination of CIS NSAs, CIS/CdS, CIS/MoS_2, and CIS/CdS/MoS_2 electrodes immersed in a solution of 0.1 M Na_2SO_4, and the equivalent fitting circuit is depicted in inset of Figure 7a, where R_S, R_{CT}, and CPE portray the electrolyte solution resistance, interfacial charge-transfer resistance at the electrode/electrolyte, and constant phase element for the photoelectrode/electrolyte, respectively. The parameters of the fitted circuit are given in Table S2 in the Supporting Information. The estimated numerical values for charge-transfer resistance (R_{CT}) of CIS NSAs, CIS/CdS, CIS/MoS_2, and CIS/CdS/MoS_2 photocathodes are 1.31, 1.1, 1.03, and 0.63 kΩ, respectively. As a result, CIS/CdS/MoS_2 showed low R_{CT} compared to CIS/CdS and CIS NSAs, indicating the facile charge separation and transportation. Additionally, the Bode phase plot represents the lifetime of the charge carriers in the excited state. The plot is —phase angle (θ) vs log(frequency)/(Hz) (Supporting Information, Figure S13), where τ is the lifetime of the electron. The τ value is measured with the equation $\tau = 1/(2\pi f_{max})$, wherein f_{max} is the frequency maximum. The calculated electron lifetimes of CIS/CdS/MoS_2, CIS/CdS, and CIS NSAs are 895, 224, and 221 ms, respectively. From Bode phase plots, the CIS/CdS/MoS_2 showed a high τ value. This behavior indicates that the deposition of MoS_2 on CIS/CdS significantly ameliorated the electron lifetime and reduced the charge recombination, which is due to the superficial electron transmission from CIS NSAs to MoS_2 via CdS. Furthermore, the Mott−Schottky plots of electrodes (Figure 7b) were plotted, where the linear profiles with a negative slope confirmed that the photoelectrodes are of p-type.[40] On the projection of intercepts on the x-axis, flat band potential (V_{FB}) was evaluated, which turned out to be 1.25, 1.22, 1.23, and 1.10 V for CIS/CdS/MoS_2, CIS/CdS, CIS/MoS_2, and CIS NSA electrodes, respectively. There is a positive shift in the V_{FB} potential for CIS/CdS/MoS_2 compared to other electrodes owing to an increase in charge carrier concentration, indicating a decrease in the bending band edge, which leads to the superficial transmission of photogenerated carriers with low recombination, thereby improving the PEC performance.[41] Moreover, from the $M-S$ plots, a smaller magnitude of the slope insinuates greater charge carrier concentration. The calculated charge carrier concentrations of CIS/CdS/MoS_2, CIS/CdS, and CIS NSAs are 3.03×10^{16} cm^{-3}, 2.14×10^{16} cm^{-3}, and 3.8×10^{15} cm^{-3}, respectively, at 100 kHz. Impressively, the CIS/CdS/MoS_2 photocathode exhibited higher charge carrier density and delivered a faster carrier transfer than the other samples, which benefits the PEC performance for the hydrogen evolution reaction. Hydrogen evolution quantification was considered to examine the effect of heterojunction formation over CIS using gas chromatography. We used CIS and CIS/CdS/MoS_2 films of 2 cm × 2 cm area, illuminated it with light for 1 h, and quantified the gas evolved (Supporting Information, Figure S14). The gas evolved from CIS/CdS/MoS_2 was 56.9 μmol while CIS exhibited 22.6 μmol after 60 min of continuous activity.

Plausible Mechanism. Schematic illustration of CIS/CdS/MoS_2 is shown in Figure 7c and the mechanism of PEC performance by the ternary photocathode CIS/CdS/MoS_2 is schematically presented in Figure 7d. Here, the simulated solar illumination of the light on the electrode leads to the generation of electron−hole pairs in the conduction band (CB) and valence bands (VB) of CIS NSAs. The VB and CB positions of CIS NSAs are −0.55 eV vs RHE and 1.07 eV vs RHE, collected from M-S plots and optical measurements (Supporting Information, Figure S8). The calculated band positions in the energy level diagram are presented in Figure 7d. The excited electrons migrate from the VB (1.07 eV vs RHE) to the CB (−0.55 eV vs RHE) of CIS NSAs. Incorporating an overlayer of n-type CdS having the CB and VB at −0.50 eV vs RHE and 1.70 eV vs RHE gives rise to a p−n junction,[42−44] resulting in the transfer of photogenerated electrons in the CIS NSA CB to CB of CdS. Then, electrons are transferred to the noble metal-free co-catalyst MoS_2 having CB and VB positions −0.23 eV vs RHE and 1.71 eV vs RHE, respectively, providing surface active sites to the H^+ ions for adsorption and getting reduced to H_2 with the photoexcited electrons.[43] The facile transfer of electrons via the cascaded process gives a better opportunity to separate electron−hole pairs and minimize recombination probability.

CONCLUSIONS

In summary, a novel heterostructure of CIS/CdS/MoS_2 photocathodes was fabricated. As a result, the CIS/CdS/MoS_2 photocathode showed excellent PEC performance compared to the pristine CIS NSA photocathode. The photocurrent density of CIS/CdS/MoS_2 enhanced over 6.6 times than pristine CIS NSAs, 2.1 times higher compared to CIS/MoS_2, and 2.2 times for CIS/CdS. Moreover, the composite showed low charge-transfer resistance and a longer electron lifetime for PEC water splitting. Incorporating an overlayer of n-type CdS creates a p−n junction, resulting in

https://doi.org/10.1021/acs.energyfuels.2c03502
Energy Fuels 2023, 37, 2340−2349

enhanced light absorption and charge carrier concentration, and facilitates the separation and transmission of electrons to the co-catalyst surface. The noble metal-free co-catalyst MoS_2 collects the electrons and provides active surface sites for HER. In addition, the layer of MoS_2 functioned as a passivation layer and imparted a stabilizing effect by minimizing the deterioration of the photoelectrode due to photocorrosion in correlation with chronoamperometric curves. This synergistic effect of CdS and MoS_2 over CIS NSAs not only increases the stability of the photoelectrode but also enhances PEC performance.

■ ASSOCIATED CONTENT

Supporting Information

The Supporting Information is available free of charge at https://pubs.acs.org/doi/10.1021/acs.energyfuels.2c03502.

Chemicals, characterization techniques, PEC measurements and equations, XRD plot, N_2 adsorption−desorption, pore size distribution of CIS NSAs, size distribution of CIS sheet width, cross-sectional SEM images, EDAX analysis, UV−vis and Tauc's graphs, band gap, VB and CB measurements, LSV curves, Mott−Schottky equations, EIS equivalent circuit parameters, Bode phase curves, hydrogen evolution, and table for comparison with the reported literature (PDF)

■ AUTHOR INFORMATION

Corresponding Author

Challapalli Subrahmanyam − *Department of Chemistry, Indian Institute of Technology Hyderabad, Hyderabad, Telangana 502285, India;* orcid.org/0000-0002-2643-3854; Phone: +91-40-23016050; Email: csubbu@iith.ac.in

Authors

Mohit Kumar − *Department of Chemistry, Indian Institute of Technology Hyderabad, Hyderabad, Telangana 502285, India*

Bhagatram Meena − *Department of Chemistry, Indian Institute of Technology Hyderabad, Hyderabad, Telangana 502285, India*

Palyam Subramanyam − *Research Institute for Electronic Science, Hokkaido University, Sapporo, Hokkaido 001-0020, Japan*

Govind Ummethala − *Department of Materials Science and Metallurgical Engineering Indian Institute of Technology, Sangareddy 502285, India*

Sai Rama Krishna Malladi − *Department of Materials Science and Metallurgical Engineering Indian Institute of Technology, Sangareddy 502285, India*

Shourya Dutta-Gupta − *Department of Materials Science and Metallurgical Engineering Indian Institute of Technology, Sangareddy 502285, India;* orcid.org/0000-0001-5680-3847

Complete contact information is available at: https://pubs.acs.org/10.1021/acs.energyfuels.2c03502

Notes

The authors declare no competing financial interest.

■ ACKNOWLEDGMENTS

M.K. and B.M. thanks CSIR-India for providing fellowship. The authors would also like to extend their special thanks to Poondla Vijayakumar for the XPS characterizations, Ranjit Kumar for the XRD characterizations, M.UmamaheshwaraRao for BET, and K.V.S.S. Bhargavi for GC analysis.

■ REFERENCES

(1) Staffell, I.; Scamman, D.; Velazquez Abad, A.; Balcombe, P.; Dodds, P. E.; Ekins, P.; Shah, N.; Ward, K. R.The Role of Hydrogen and Fuel Cells in the Global Energy System. *Energy and Environmental Science*; The Royal Society of Chemistry February, 2019; Vol. *12*, pp 463−491.

(2) Fujishima, A.; Honda, K. Electrochemical Photolysis of Water at a Semiconductor Electrode. *Nature* **1972**, *238*, 37−38.

(3) Qiu, Y.; Pan, Z.; Chen, H.; Ye, D.; Guo, L.; Fan, Z.; Yang, S. Current Progress in Developing Metal Oxide Nanoarrays-Based Photoanodes for Photoelectrochemical Water Splitting. *Sci. Bull.* **2019**, *64*, 1348−1380.

(4) Meena, B.; Kumar, M.; Gupta, S.; Sinha, L.; Subramanyam, P.; Subrahmanyam, C. Rational Design of TiO2/BiSbS3 Heterojunction for Efficient Solar Water Splitting. *Sustain. Energy Technol. Assessments* **2022**, *49*, 101775.

(5) Kumar, M.; Meena, B.; Subramanyam, P.; Suryakala, D.; Subrahmanyam, C. Emerging Copper-Based Semiconducting Materials for Photocathodic Applications in Solar Driven Water Splitting. *Catalysts* **2022**, *12*, 1198.

(6) Kumar, M.; Ghosh, C. C.; Meena, B.; Ma, T.; Subrahmanyam, C. Plasmonic Au Nanoparticle Sandwiched CuBi 2 O 4 /Sb 2 S 3 Photocathode with Multi-Mediated Electron Transfer for Efficient Solar Water Splitting. *Sustainable Energy Fuels* **2022**, *6*, 3961−3974.

(7) Leach, A. D. P.; Macdonald, J. E. Optoelectronic Properties of CuInS2 Nanocrystals and Their Origin. *J. Phys. Chem. Lett.* **2016**, *7*, 572−583.

(8) Gunawan; Haris, A.; Widiyandari, H.; Septina, W.; Ikeda, S.Surface Modifications of Chalcopyrite CuInS2 Thin Films for Photochatodes in Photoelectrochemical Water Splitting under Sunlight Irradiation. *IOP Conference Series: Materials Science and Engineering*; IOP Publishing, 2017; Vol. *172*, p 012021.

(9) Kang, D.; Hill, J. C.; Park, Y.; Choi, K. S. Photoelectrochemical Properties and Photostabilities of High Surface Area CuBi2O4 and Ag-Doped CuBi2O4 Photocathodes. *Chem. Mater.* **2016**, *28*, 4331−4340.

(10) Li, M.; Zhao, R.; Su, Y.; Hu, J.; Yang, Z.; Zhang, Y. Hierarchically CuInS 2 Nanosheet-Constructed Nanowire Arrays for Photoelectrochemical Water Splitting. *Adv. Mater. Interfaces* **2016**, *3*, 1600494.

(11) Moniz, S. J. A.; Shevlin, S. A.; Martin, D. J.; Guo, Z.-X.; Tang, J. Visible-Light Driven Heterojunction Photocatalysts for Water Splitting − a Critical Review. *Energy Environ. Sci.* **2015**, *8*, 731−759.

(12) Bhat, S. S. M.; Pawar, S. A.; Potphode, D.; Moon, C. K.; Suh, J. M.; Kim, C.; Choi, S.; Patil, D. S.; Kim, J. J.; Shin, J. C.; Jang, H. W. Substantially Enhanced Photoelectrochemical Performance of TiO2 Nanorods/CdS Nanocrystals Heterojunction Photoanode Decorated with MoS2 Nanosheets. *Appl. Catal., B* **2019**, *259*, 118102.

(13) Li, D.; Shi, J.; Li, C. Transition-Metal-Based Electrocatalysts as Cocatalysts for Photoelectrochemical Water Splitting: A Mini Review. *Small* **2018**, *14*, 1704179.

(14) Yang, W.; Oh, Y.; Kim, J.; Kim, H.; Shin, H.; Moon, J. Photoelectrochemical Properties of Vertically Aligned CuInS 2 Nanorod Arrays Prepared via Template-Assisted Growth and Transfer. *ACS Appl. Mater. Interfaces* **2016**, *8*, 425−431.

(15) Cai, Q.; Liu, Z.; Han, C.; Tong, Z.; Ma, C. CuInS2/Sb2S3 Heterostructure Modified with Noble Metal Co-Catalyst for Efficient Photoelectrochemical Water Splitting. *J. Alloys Compd.* **2019**, *795*, 319−326.

(16) Sun, B.; Shan, F.; Jiang, X.; Ji, J.; Wang, F. One-Pot Synthesis of MoS 2 /In 2 S 3 Ultrathin Nanoflakes with Mesh−shaped Structure on Indium Tin Oxide as Photocathode for Enhanced Photo-and Electrochemical Hydrogen Evolution Reaction. *Appl. Surf. Sci.* **2018**, *435*, 822−831.

(17) Meena, B.; Subramanyam, P.; Suryakala, D.; Biju, V.; Subrahmanyam, C. Efficient Solar Water Splitting Using a CdS Quantum Dot Decorated TiO2/Ag2Se Photoanode. *Int. J. Hydrogen Energy* **2021**, *46*, 34079−34088.
(18) Li, M.; Chen, L.; Su, Y.; Yin, H.; Hu, K. Hexagonally Ordered Microbowl Arrays Decorated with Ultrathin CuInS2 Nanosheets for Enhanced Photoelectrochemical Performance. *J. Energy Chem.* **2020**, *51*, 134−142.
(19) Zhao, J.; Minegishi, T.; Kaneko, H.; Ma, G.; Zhong, M.; Nakabayashi, M.; Hisatomi, T.; Katayama, M.; Shibata, N.; Yamada, T.; Domen, K. Efficient Hydrogen Evolution on (CuInS2): X(ZnS)1-x Solid Solution-Based Photocathodes under Simulated Sunlight. *Chem. Commun.* **2019**, *55*, 470−473.
(20) Subramanyam, P.; Meena, B.; Neeraja Sinha, G.; Suryakala, D.; Subrahmanyam, C. Facile Synthesis and Photoelectrochemical Performance of a Bi2S3@rGO Nanocomposite Photoanode for Efficient Water Splitting. *Energy Fuel.* **2021**, *35*, 6315−6321.
(21) Jiang, F.; Gunawan; Harada, T.; Kuang, Y.; Minegishi, T.; Domen, K.; Ikeda, S. Pt/In 2 S 3 /CdS/Cu 2 ZnSnS 4 Thin Film as an Efficient and Stable Photocathode for Water Reduction under Sunlight Radiation. *J. Am. Chem. Soc.* **2015**, *137*, 13691−13697.
(22) Li, M.; Zhao, R.; Su, Y.; Hu, J.; Yang, Z.; Zhang, Y. Synthesis of CuInS2 Nanowire Arrays via Solution Transformation of Cu2S Self-Template for Enhanced Photoelectrochemical Performance. *Appl. Catal., B* **2017**, *203*, 715−724.
(23) Septina, W.; Prabhakar, R. R.; Wick, R.; Moehl, T.; Tilley, S. D. Stabilized Solar Hydrogen Production with CuO/CdS Heterojunction Thin Film Photocathodes. *Chem. Mater.* **2017**, *29*, 1735−1743.
(24) Zhan, Y.; Shao, Z.; Jiang, T.; Ye, J.; Wu, X.; Zhang, B.; Ding, K.; Wu, D.; Jie, J. Cation Exchange Synthesis of Two-Dimensional Vertical Cu 2 S/CdS Heterojunctions for Photovoltaic Device Applications. *J. Mater. Chem. A* **2020**, *8*, 789−796.
(25) Zhou, Y.; Shin, D.; Ngaboyamahina, E.; Han, Q.; Parker, C. B.; Mitzi, D. B.; Glass, J. T. Efficient and Stable Pt/TiO 2 /CdS/Cu 2 BaSn(S,Se) 4 Photocathode for Water Electrolysis Applications. *ACS Energy Lett.* **2018**, *3*, 177−183.
(26) Reichert, R.; Jusys, Z.; Behm, R. J. Au/TiO2 Photo(Electro)-Catalysis: The Role of the Au Cocatalyst in Photoelectrochemical Water Splitting and Photocatalytic H2 Evolution. *J. Phys. Chem. C* **2015**, *119*, 24750−24759.
(27) Tilley, S. D.; Schreier, M.; Azevedo, J.; Stefik, M.; Graetzel, M. Ruthenium Oxide Hydrogen Evolution Catalysis on Composite Cuprous Oxide Water-Splitting Photocathodes. *Adv. Funct. Mater.* **2014**, *24*, 303−311.
(28) Liu, Z.; Zhou, M. Co-Modification with Cost-Effective Nickel Oxides and Nickel Sulfides on CuInS 2 Nanosheets Photocathode for Enhanced Photoelectrochemical Performance. *ACS Sustainable Chem. Eng.* **2020**, *8*, 512−519.
(29) Kumar, M.; Meena, B.; Subramanyam, P.; Suryakala, D.; Subrahmanyam, C. Recent Trends in Photoelectrochemical Water Splitting: The Role of Cocatalysts. *NPG Asia Mater.* **2022**, *14*, 88.
(30) Dolai, S.; Maiti, P.; Ghorai, A.; Bhunia, R.; Paul, P. K.; Ghosh, D. Exfoliated Molybdenum Disulfide-Wrapped CdS Nanoparticles as a Nano-Heterojunction for Photo-Electrochemical Water Splitting. *ACS Appl. Mater. Interfaces* **2021**, *13*, 438−448.
(31) King, L. A.; Hellstern, T. R.; Park, J.; Sinclair, R.; Jaramillo, T. F. Highly Stable Molybdenum Disulfide Protected Silicon Photocathodes for Photoelectrochemical Water Splitting. *ACS Appl. Mater. Interfaces* **2017**, *9*, 36792−36798.
(32) Ding, Q.; Song, B.; Xu, P.; Jin, S. Efficient Electrocatalytic and Photoelectrochemical Hydrogen Generation Using MoS2 and Related Compounds. *Chem* **2016**, *1*, 699−726.
(33) Yuan, Y.-J.; Chen, D.-Q.; Huang, Y.-W.; Yu, Z.-T.; Zhong, J.-S.; Chen, T.-T.; Tu, W.-G.; Guan, Z.-J.; Cao, D.-P.; Zou, Z.-G. MoS 2 Nanosheet-Modified CuInS 2 Photocatalyst for Visible-Light-Driven Hydrogen Production from Water. *ChemSusChem* **2016**, *9*, 1003−1009.
(34) Qin, S.; Li, K.; Zhu, J.; Xu, H.; Ali, N.; Rahimi-Iman, A.; Wu, H. A New Strategy to Improve the Performance of MoS2-Based 2D Photodetector by Synergism of Colloidal CuInS2 Quantum Dots and Surface Plasma Resonance of Noble Metal Nanoparticles. *J. Alloys Compd.* **2021**, *856*, 158179.
(35) Varunkumar, K.; Sellappan, R. Photoelectrochemical Behaviour of CuBi2O4@MoS2 Photocathode for Solar Water Splitting. *Mater. Chem. Phys.* **2021**, *261*, 124245.
(36) Cai, Q.; Liu, Z.; Ma, C.; Tong, Z.; Han, C. Network-like CuInS2 Photocathode and Modified with Noble Metal Co-Catalyst for Photoelectrochemical Water Splitting. *J. Mater. Sci.: Mater. Electron.* **2018**, *29*, 20629−20638.
(37) Zhai, C.; Zhu, M.; Pang, F.; Bin, D.; Lu, C.; Goh, M. C.; Yang, P.; Du, Y. High Efficiency Photoelectrocatalytic Methanol Oxidation on CdS Quantum Dots Sensitized Pt Electrode. *ACS Appl. Mater. Interfaces* **2016**, *8*, 5972−5980.
(38) Zhang, S.; Liu, X.; Liu, C.; Luo, S.; Wang, L.; Cai, T.; Zeng, Y.; Yuan, J.; Dong, W.; Pei, Y.; Liu, Y. MoS2 Quantum Dot Growth Induced by S Vacancies in a ZnIn2S4 Monolayer: Atomic-Level Heterostructure for Photocatalytic Hydrogen Production. *ACS Nano* **2018**, *12*, 751−758.
(39) Zheng, Z.; Qiao, Y.; Cai, Y.; He, Y.; Tang, Y.; Li, L. MoS2 Decorated CdS Hybrid Heterojunction for Enhanced Photoelectrocatalytic Performance under Visible Light Irradiation. *J. Colloid Interface Sci.* **2019**, *533*, 561−568.
(40) Lu, C.; Ma, Z.; Jäger, J.; Budnyak, T. M.; Dronskowski, R.; Rokicińska, A.; Kuśtrowski, P.; Pammer, F.; Slabon, A. NiO/Poly(4-Alkylthiazole) Hybrid Interface for Promoting Spatial Charge Separation in Photoelectrochemical Water Reduction. *ACS Appl. Mater. Interfaces* **2020**, *12*, 29173−29180.
(41) Zhang, F.; Chen, Y.; Zhou, W.; Ren, C.; Gao, H.; Tian, G. Hierarchical SnS 2 /CuInS 2 Nanosheet Heterostructure Films Decorated with C 60 for Remarkable Photoelectrochemical Water Splitting. *ACS Appl. Mater. Interfaces* **2019**, *11*, 9093−9101.
(42) Wei, Y.; He, H.; Liu, C.; Yang, L.; Wang, X.; Li, A.; Xiong, Y.; Shen, Q.; Zhou, Y.; Zou, Z. α-Fe2O3/Ag/CdS Ternary Heterojunction Photoanode for Efficient Solar Water Oxidation. *Catal. Sci. Technol.* **2021**, *11*, 5859−5867.
(43) Lin, L.; Huang, S.; Zhu, Y.; Du, B.; Zhang, Z.; Chen, C.; Wang, X.; Zhang, N. Construction of CdS/MoS 2 Heterojunction from Core-Shell MoS 2 @Cd-MOF for Efficient Photocatalytic Hydrogen Evolution. *Dalton Trans.* **2019**, *48*, 2715−2721.
(44) Meena, B.; Kumar, M.; Kumar, A.; Sinha, G. N.; Nagumothu, R.; Subramanyam, P.; Suryakala, D.; Subrahmanyam, C. Integrated P-n Junctions for Efficient Solar Water Splitting upon TiO2/CdS/BiSbS3 Ternary Hybrids for Improved Hydrogen Evolution and Mechanistic Insights. *Catalysts* **2022**, *12*, 1117.

https://doi.org/10.1021/acs.energyfuels.2c03502
Energy Fuels 2023, 37, 2340−2349